Jurnal Ilmu Fisika
Vol. 19, No. 1, March 2027, pp. 40–52
ISSN: 1979-4657 (Print); 2614-7386 (Online)
https://doi.org/10.25077/jif.19.1.40-52.2027

Jurnal Ilmu Fisika
Open Access

Fabrication of a Beeswax-Based Chest Phantom Incorporating *Anadara antiquata* Shell-Derived $CaCO_3$ for Adult Lung Cancer Simulation

Ardilah Ardilah[1], Choirul Anam[1], Ilham Alkian[3], Heri Sutanto[1,2*], Nurul Sabihah Zakaria[4]

[1]Department of Physics, Faculty of Sciences and Mathematics, Diponegoro University, Semarang 50275, Indonesia
[2]Smart Material Research Center (SMARC), Diponegoro University, Semarang 50275, Indonesia
[3]Research Center for Nanotechnology System, National Research and Innovation Agency (BRIN), South Tangerang 15314, Indonesia
[4]Physics Section, School of Distance Education, Universiti Sains Malaysia (USM), Pulau Pinang 11800, Malaysia

Article Info

Article History:

Received July 14, 2026
Revised October 31, 2026
Accepted October 31, 2026
Published November 08, 2026

Keywords:

lung cancer
chest phantom
radiodiagnostic
thoracic CT
image quality

Corresponding Author:

Heri Sutanto,
Email: herisutanto@live.undip.ac.id

ABSTRACT

Lung cancer remains a major cause of cancer mortality, while chest CT requires careful radiation dose optimization. Commercial anthropomorphic phantoms are costly, and shell-derived bone substitutes for chest phantoms with simulated pulmonary nodules remain insufficiently evaluated. This study developed and assessed a low-cost adult chest phantom using locally available materials: polymethyl methacrylate (PMMA) for soft tissue, polyurethane (PU) foam for lung tissue, calcium carbonate derived from Anadara antiquata shell waste for bone, and beeswax for a simulated pulmonary nodule. The phantom was scanned using a 128-slice Multi-Slice Computed Tomography (MSCT) scanner with Automatic Exposure Control (AEC) at 80, 100, and 120 kV. Radiometric performance was evaluated using CT numbers, Signal-to-Noise Ratio (SNR), and Contrast-to-Noise Ratio (CNR). Measured CT numbers were −62.59 ± 17.59 HU for beeswax, −915.34 ± 15.65 HU for lung tissue, 113.48 ± 14.64 HU for soft tissue, and 1155.35 ± 170.70 HU for bone. These values were compared with published tissue attenuation ranges. The phantom shows potential for CT image quality assessment and optimization, although further validation is needed to improve lesion representation and establish broader clinical applicability. This approach also explores the reuse of shell waste.

Copyright © 2026 Author(s)

1. INTRODUCTION

Cancer, characterized by the uncontrolled growth and spread of abnormal cells, remains a major health challenge (Hassan et al., 2026). Among all cancer types, lung cancer is one of the deadliest, accounting for nearly 27% of cancer-related deaths worldwide (World Health Organization, 2023). Timely diagnosis enables less invasive and prompt interventions, whereas delayed detection often results in advanced-stage disease with limited treatment options (Sung et al., 2021). Computed tomography (CT) is considered the standard imaging modality for the early detection, staging, and follow-up evaluation of both small cell lung cancer (SCLC) and non-small cell lung cancer (NSCLC) (Frellesen et al., 2016).

In the evaluation of lung cancer, chest CT provides superior diagnostic performance because it produces clearer pathological images, thereby enabling the detection of abnormalities that may

Attribution-NonCommercial 4.0 International

otherwise be overlooked (Sawall et al., 2025). The radiation dose associated with CT scans typically ranges from 1 to 14 mSv, depending on the examination, which is comparable to the annual dose received from natural radiation sources, such as radon and cosmic radiation (1–10 mSv) (McCollough et al., 2009). These values depend on the scanning protocol and patient characteristics, with the resulting effective dose range determined by the selection of scanning parameters at each facility (Larke et al., 2011). Although CT plays a crucial role in the diagnosis of pulmonary diseases, the associated radiation exposure may increase the risk of developing cancer in the future. Therefore, radiation protection for patients must be improved, and careful attention should be given to the administration of appropriate radiation doses (Fu et al., 2025). Radiation dose optimization is crucial in CT scanning to ensure that patients receive the lowest reasonably achievable radiation dose without compromising diagnostic image quality (Goo, 2012).

Phantoms are widely used in CT radiation dose optimization studies because of their ability to simulate the characteristics of human tissues. This enables practitioners to perform CT scan simulations accurately without directly involving patients, making radiation dose optimization studies safer and more efficient (Bushberg et al., 2012). However, commercially available chest phantoms are expensive, limiting their accessibility for many institutions. In addition, only a limited number of commercially available phantoms are capable of replicating lung cancer conditions. Studies focusing on the fabrication of lung cancer phantoms also remain scarce. Therefore, the development of a chest phantom capable of replicating lung cancer using affordable and readily available materials is of considerable importance.

Several previous studies have investigated materials for chest phantom fabrication. One such material is cork, which has been used as a substitute for human lung tissue (Mohammed Ali & Al-Murshedi, 2023). However, cork is susceptible to mechanical degradation due to environmental factors such as humidity and temperature (Sergi et al., 2022). As an alternative, several studies have used polyurethane (PU) foam as a substitute for lung tissue (Amini et al., 2018; Jamal et al., 2020). PU foam is considered more advantageous because its density is more similar to that of human lung tissue and it is more readily available in Indonesia than cork (Jamal et al., 2020).

In a subsequent study, resin was used as one of the primary materials for chest phantom fabrication. Pengpan et al. (2022) developed an in-house pediatric chest phantom based on resin to evaluate image quality and radiation dose in chest radiography examinations (Pengpan et al., 2022). Nevertheless, this study focused on pediatric applications and the radiography modality rather than adult chest phantoms for CT evaluation. Resin is known for its high precision in simulating soft tissue. However, the fabrication process may involve several stages, such as mixing, molding, curing, and dimensional control, which can increase production complexity and associated costs (Mohammed Ali & Al-Murshedi, 2023). Currently, PMMA remains one of the most widely used materials for soft tissue simulation in phantom fabrication. PMMA is preferred because of its transparency, tissue-equivalent properties, and ease of processing, which facilitates a more efficient fabrication process (Khallouqi et al., 2024a; Khallouqi et al., 2024b). Furthermore, a study by Heryani et al. showed that a mixture of calcium carbonate ($CaCO_3$) and polyester resin (PR) was effective in representing human bone, with CT numbers ranging from +100 HU to +1000 HU (Heryani et al., 2020).

Previous studies have not specifically evaluated the use of $CaCO_3$ powder derived from *Anadara antiquata* shell waste for the fabrication of adult chest phantoms for CT imaging. Studies on shell-derived calcium have primarily focused on its chemical and structural characterization and its potential applications as a biomaterial, rather than its use in phantoms for simulating lung cancer or pulmonary nodules. Therefore, this study developed an in-house adult chest phantom using $CaCO_3$ derived from *Anadara antiquata* shell waste, PMMA as a soft-tissue substitute, and beeswax as a surrogate material for lung cancer or pulmonary nodules. Unlike studies focused on pediatric radiography phantoms or conventional synthetic bone substitutes, the present work evaluates a shell-derived $CaCO_3$–polyester-resin rib component together with a beeswax nodule in a modular adult CT phantom. The objective is to assess whether this specific material combination produces tissue-relevant CT attenuation and measurable nodule-to-lung contrast, rather than to establish clinical equivalence. The phantom was subsequently evaluated based on the CT number, signal-to-noise ratio (SNR), and contrast-to-noise ratio (CNR) at several tube voltages.

On the other hand, *Anadara antiquata* shells originating from the coastal regions of Sumatra represent a type of shell waste with potential for use as a calcium-based material source. Shells generally contain high amounts of calcium carbonate, making them a potential alternative raw material for various material applications. Pratama and Widayanti (2025) reported the potential of *Anadara antiquata* shells as a calcium-based material. However, the chemical composition of shells may vary depending on the species, location, and characterization method (Pratama & Widayanti, 2025). In this study, *Anadara antiquata* shells were directly characterized using Energy-Dispersive X-ray Spectroscopy (EDX). The analysis revealed a Ca elemental concentration of 97.86%, reflecting the calcium content within the material matrix. This finding indicates that *Anadara antiquata* shells have considerable potential as a calcium-rich material source for fabricating the bone-equivalent component of an in-house chest phantom.

This study addresses the limited evaluation of shell-derived $CaCO_3$ powder as a bone-substitute component in adult chest CT phantoms incorporating pulmonary nodule simulation. By combining $CaCO_3$ powder derived from *Anadara antiquata* shells with polyester resin, PMMA, PU foam, and beeswax, this study evaluated the CT attenuation characteristics of the fabricated phantom and its image quality performance across different tube voltage settings. This study was intended to provide an initial physical assessment of the material combination rather than to establish its clinical equivalence to human lung cancer.

2. MATERIALS AND METHODS

This study did not involve human or animal participants. The study was conducted using a phantom, and no consent was obtained from participants.

2.1 Phantom Design

Two important aspects that must be considered in the fabrication of a chest phantom are its size and design. Both should be adjusted to accurately represent the anatomical characteristics of the tissue being simulated. In this study, the chest phantom was designed with axial slices of 10 mm thickness and dimensions of 300 mm × 200 mm. The right and left lung cavities were designed with dimensions of 80 mm × 120 mm each. These dimensions were based on standard adult cross-sectional anatomical guidelines (standard anthropomorphic specifications) for the adult population (reference age of 18 years and older). The anatomical outlines were proportionally scaled using vector-based scaling and designed in CorelDRAW to produce laser-cut PMMA layers. This design represents a simplified adult-sized thoracic geometry and is not specifically tailored to any particular sex or body habitus, referring to the commercial specifications provided by QRM (QRM GmbH, Mohrendorf, Germany) (QRM GmbH, 2020). This target geometry and population are further supported by clinical measurements of thoracic dimensions in young adults (Nathan et al., 2021). The phantom consists of 12 modular slices, each 10 mm thick, arranged sequentially from bottom to top following a layered phantom fabrication technique (Rodgers et al., 2024). The phantom design was developed using CorelDRAW software. In addition to the phantom size and design, careful consideration must also be given to material selection, as the chosen materials should be capable of replicating the radiological characteristics of human tissues while maintaining these properties over an extended period.

2.2 Phantom Fabrication

In this study, the chest phantom was fabricated using PMMA as a soft tissue substitute (Amini et al., 2018; Mohammed Ali & Al-Murshedi, 2023), $CaCO_3$ as a rib substitute (Heryani et al., 2020), and PU foam as a lung tissue substitute (Pengpan et al., 2022; Jamal et al., 2020). The lung cancer lesion observed in the patient was replicated using beeswax. The selection of tissue-equivalent materials was based on the similarity of their radiological attenuation characteristics, effective atomic number (Z_{eff}) and electron density, as reflected by the Hounsfield Unit (HU) values on CT images (Amini et al., 2018; Nisa et al., 2025). These values are presented in Table 1. Table 1 lists the densities of the pure materials as theoretical reference values, whereas the phantom rib material was fabricated as a composite

mixture of $CaCO_3$ powder derived from *Anadara antiquata* shells and polyester resin. This mixing process produces a specifically tailored effective density and bulk density of the composite to reproduce the X-ray attenuation characteristics and HU values of bone, thereby establishing a clear distinction between the intrinsic density of the pure materials and the effective density of the molded composite.

Table 1. Density of tissue and tissue substitute material (Amini et al., 2018; Jamal et al., 2020; Nisa et al., 2025)

Real tissue	Organ density (g.cm^{-3})	Substitute materials	Organ density (g.cm^{-3})
Soft tissue	1.04	PMMA	1.17
Lungs	0.26	PU foam	0.30
Ribs (Bone)	1.41	$CaCO_3$	2.71
Cancer/nodule	1.06	$CaCO_3$ *Anadara antiquata*	2.60
		Beeswax	0.96

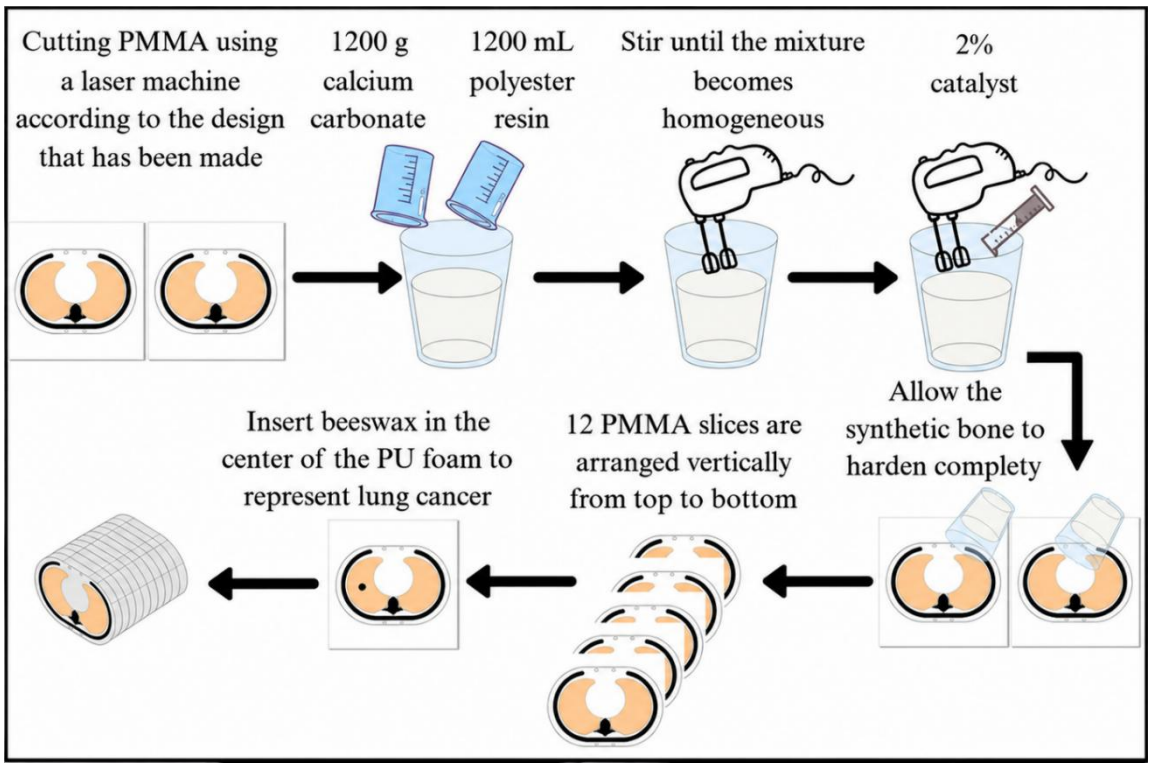


Figure 1. Chest phantom fabrication process.

Figure 1 illustrates the fabrication procedure of the chest phantom. Initially, twelve PMMA sheets, each 10 mm thick, were laser-cut according to the adult thoracic cross-sectional geometry design (reference age of 18 years, with external dimensions of 300 mm × 200 mm and right and left lung cavity dimensions of 80 mm × 120 mm), which was developed using CorelDRAW software. For the rib and vertebral components, a composite material was prepared using a total of 1200 g of $CaCO_3$ powder and 1200 mL of polyester resin to fabricate the 12 PMMA slices. Each PMMA slice required 100 g of $CaCO_3$ powder and 100 mL of resin, corresponding to a 1:1 mass-to-volume ratio. $CaCO_3$ powder was obtained from *Anadara antiquata* shell waste, which was washed, dried, crushed, and sieved through a 100-mesh sieve. For each batch, the polyester resin and $CaCO_3$ powder were measured and weighed (100 mL of resin, equivalent to 92.1 g, was mixed with 100 g of $CaCO_3$ powder). The mixture was then homogenized using a mechanical mixer for 20 minutes. Subsequently, the resin catalyst was added at a concentration of 2% (2 mL) at the end of the mixing process, followed by an additional 5 minutes of mixing. The composite mixture was then poured into the rib and vertebral molds made of silicone rubber and left at

room temperature for 24 hours to allow complete curing. After curing, the rib and vertebral composites were removed from the molds and fitted into the corresponding cavities in all 12 PMMA sheets. Once the rib and vertebral components were in place, the twelve PMMA sheets were assembled sequentially from bottom to top.

To simulate lung tissue, PU foam with a density of 0.30 $g.cm^{-3}$ was poured directly into the lung cavities of the assembled PMMA structure and allowed to expand fully. After the PU foam had cured, the PMMA assembly was disassembled to remove the PU foam (lung components). To simulate a pulmonary nodule, a cylindrical beeswax nodule with a diameter of 10 mm, a height of 10 mm, and a volume of 785.4 mm^3 was embedded in the lower region of the left lung by creating a corresponding cylindrical cavity in the PU foam. The 10 mm nodule size was selected based on the clinical threshold for high-risk solid pulmonary nodules (Anderson & Davis, 2018) as well as physical considerations to minimize the partial volume effect (PVE) during CT image reconstruction at slice thicknesses of 1–5 mm (Bushberg et al., 2012). Finally, after the nodule lesion was precisely embedded in the PU foam, all 12 PMMA sheets were reassembled sequentially from bottom to top according to their anatomical positions to form a complete chest phantom ready for use.

2.3 Data Acquisition

The chest phantom was scanned using a 128-slice Multi-Slice Computed Tomography (MSCT) scanner in helical acquisition mode. The Automatic Exposure Control (AEC) system was enabled during scanning to dynamically modulate the tube current for each slice. Scanning was performed at three tube voltages, namely 80, 100, and 120 kV, with the corresponding exposed tube current ranges of 98-100 mA at 80 kV, 108-110 mA at 100 kV, and 115-116 mA at 120 kV. The acquisition and reconstruction parameters included a rotation time of 0.8 s, a pitch of 0.98, a field of View (FOV) of 230 mm, and an image matrix of 512 × 512 pixels. The images were reconstructed using the standard B31f convolution kernel with a slice thickness of 1 mm. The radiation dose, as reported in the DICOM dose report, was indicated by $CTDI_{vol}$ values of 0.89 mGy at 80 kV, 1.89 mGy at 100 kV, and 3.46 mGy at 120 kV. The dose-length product (DLP) was calculated by multiplying $CTDI_{vol}$ by the total phantom scan length of 300 mm (30 cm). This selection was made because variations in X-ray energy can affect the computed tomography (CT) numbers of the scanned materials (Dance et al., 2014).

2.4 CT Number Validation

The CT numbers (HU) of the phantom materials were evaluated using IndoQCT software by placing circular regions of interest (ROIs) with a diameter of 10 pixels (4.5 mm) within the PMMA, rib-equivalent composite, PU foam, and beeswax regions of the reconstructed DICOM images. Specifically, the CT numbers of the phantom materials were validated at a tube voltage of 120 kV and compared with literature-derived CT number values. The ROIs were positioned within the respective materials to minimize boundary-related partial-volume effects. For the beeswax insert, the ROI was centered within the cylindrical lesion. The software-derived mean CT number and pixel standard deviation were recorded for each ROI. The standard deviation represents pixel variability within the ROI rather than variability across independent experimental replicates.

2.5 Evaluation of SNR and CNR

SNR and CNR were evaluated using 15 reconstructed CT images, comprising five axial slices acquired at each tube voltage (80, 100, and 120 kV). For each image, two circular ROIs with a diameter of 10 pixels (4.5 mm) were manually positioned using IndoQCT software. The object ROI was placed at the center of the beeswax insert, while the background ROI was positioned within the adjacent PU foam region without overlapping the lesion boundary. The nominal positions, anatomical coordinates, and ROI dimensions were consistently maintained across all three tube voltage settings. SNR and CNR were calculated separately for each slice, and the five measurements obtained at each voltage were averaged. Figure 2(b) illustrates the object and background ROI placement.

The SNR and CNR were calculated using Equations (1) and (2), respectively, in accordance with standard CT image quality assessment methods (Bushberg et al., 2012; Kamal et al., 2022; Greffier et al., 2016; Novitasari et al., 2024; Rahmawati et al., 2024).

$$SNR = \frac{|HU_{nodule}|}{\sigma_{nodule}} \quad (1)$$

$$CNR = \frac{|HU_{nodule} - HU_{background}|}{\sqrt{\frac{\sigma^2_{nodule} + \sigma^2_{background}}{2}}} \quad (2)$$

where HU_{nodule} and $HU_{background}$ represent the mean HU values within the object ROI (lung nodule) and background ROI (PU foam), respectively. Meanwhile, σ_{nodule} and $\sigma_{background}$ represent the pixel standard deviations, or noise levels, within the object and background ROIs, respectively, while $\sigma_{combination}$ or (σ_{nodule} and $\sigma_{background}$) represents the pixel standard deviation within the respective ROIs. Because the beeswax nodule exhibits a negative CT number, the absolute value operator was explicitly applied in Equation (1), in accordance with the established convention reported in the literature (Greffier et al., 2016) to yield positive SNR magnitudes.

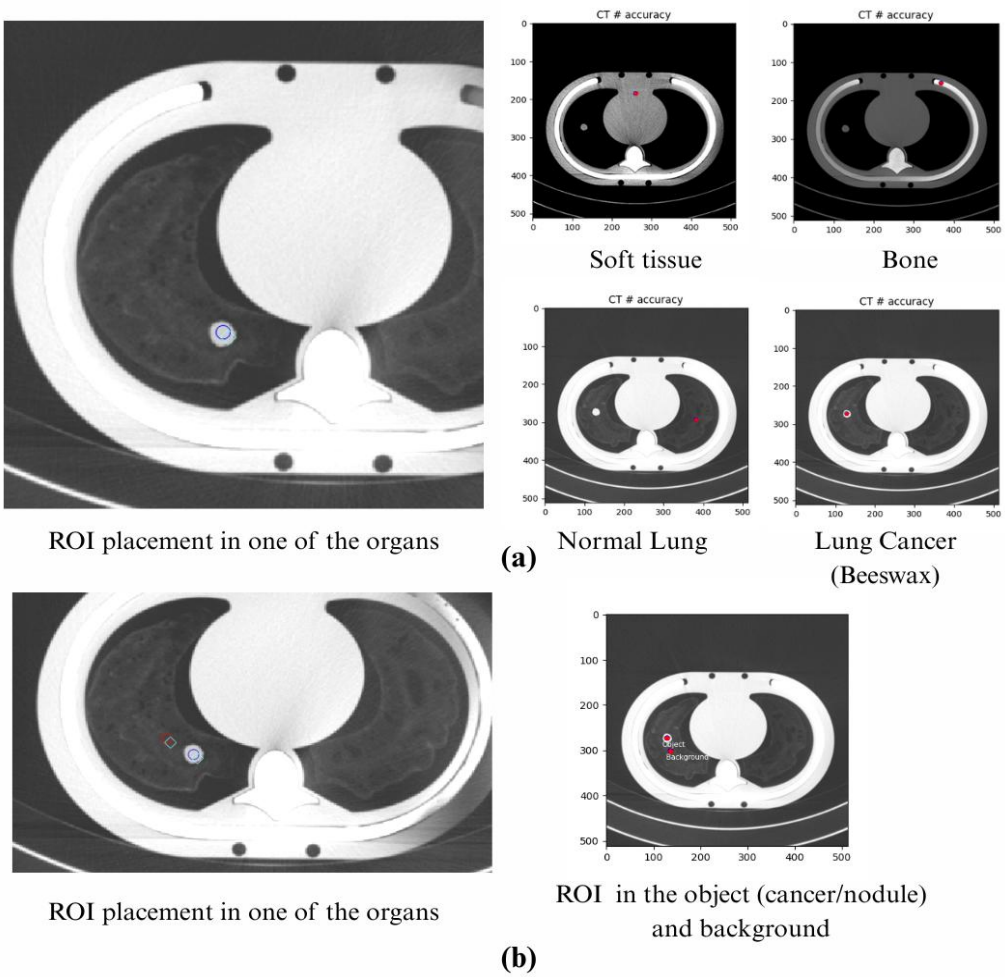


Figure 2. ROI placement in the IndoQCT software: (a) ROIs placed on the soft tissue, bone, normal lung, and lung cancer (beeswax) regions to obtain the HU values of each anatomical structure; and (b) ROI placement on the object and background to obtain the SNR and CNR values.

3. RESULTS AND DISCUSSION

3.1 Results

A chest phantom incorporating $CaCO_3$ derived from *Anadara antiquata* shell waste was successfully fabricated. Figure 3 presents the fabricated chest phantom: (a) top view, (b) front view, and (c) side view.

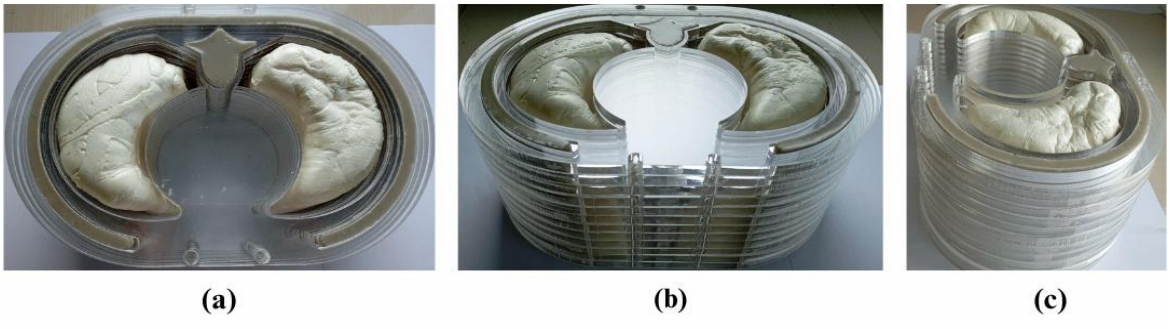


Figure 3. Fabricated chest phantom: (a) top view, (b) front view, and (c) side view.

Figure 4 shows the CT images of the fabricated chest phantom. The images were displayed using the lung window setting, which enables clearer visualization of lung cancer lesions. As shown in the axial image, the simulated lung cancer lesion appears as a distinct white circular region within the left lung. This high-density region represents the beeswax insert and exhibits strong contrast relative to the surrounding normal lung region. Figure 5 shows axial images of the chest phantom acquired at tube voltages of 80, 100, and 120 kV. Visual inspection indicates that increasing the tube voltage from 80 kV to 120 kV affects image contrast. The voltage variations result in changes in SNR and CNR values, as presented in Table 3, reflecting the radiation attenuation characteristics of the phantom structures.

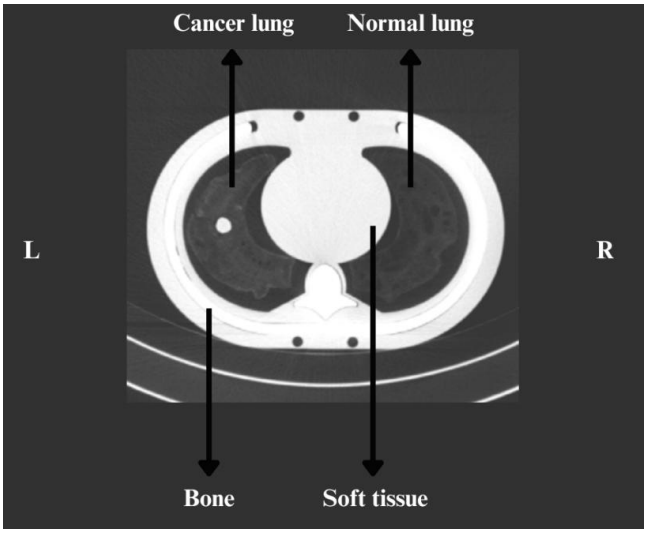


Figure 4. CT image of the fabricated chest phantom displayed using the lung window setting.

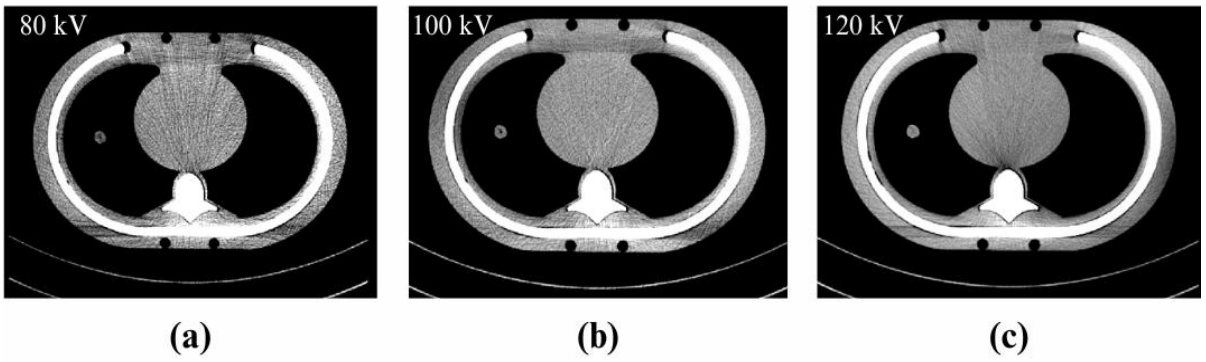


Figure 5. Axial CT images of the fabricated chest phantom acquired at different tube voltages: (a) 80 kV, (b) 100 kV, and (c) 120 Kv.

3.1.1 CT Number

The CT numbers obtained from the literature-reported patient reference image and the fabricated phantom are presented in Table 2. The results indicate that the CT numbers of PMMA, $CaCO_3$ derived from *Anadara antiquata* shell waste, and PU foam fall within the corresponding CT number ranges of soft tissue, bone, and normal lung tissue, respectively. In contrast, the CT number of beeswax was found to be close to that of the lung cancer lesion in the patient reference images.

Table 2. Comparison between the human thoracic reference ranges reported in the literature and the CT number measurements obtained from the fabricated chest phantom

Real tissue	Substitute materials	Literature reference CT number (HU)	Fabricated Chest phantom CT number (HU)
Soft tissue	PMMA	110 to 135 (Sookpeng et al., 2016)	113.48 ± 14.64
Ribs (Bone)	$CaCO_3$ *Anadara antiquata*	662 to 1988 (Hong et al., 2023)	1155.35 ± 170.70
Normal lung	PU Foam	-950 to -600 (Nisa et al., 2025; Hong et al., 2023)	-915.34 ± 15.65
Lung Cancer	Beeswax	-100 to 200 (Swensen et al., 2000; Choi et al., 2019)	-62.59 ± 17.59

As shown in Table 2, PMMA was used as a soft-tissue substitute. During measurement, the ROI was positioned within the main body of the thoracic phantom. The results showed that the CT number of PMMA (113.48 ± 14.64 HU) fell within the literature-reported reference range for soft tissue (Sookpeng et al., 2016).

3.1.2 SNR and CNR

The SNR and CNR values are presented in Table 3 and Figure 6. The SNR and CNR values were obtained from the analysis of 15 chest phantom images, consisting of five slices at each tube voltage (80, 100, and 120 kV). Each slice was analyzed using one pair of ROIs, consisting of an object ROI (nodule/beeswax) and a background ROI positioned outside the nodule. The values for ROI 1, ROI 2, ROI 3, ROI 4, and ROI 5 represent the measurement results obtained from one slice for each tube voltage variation, with the same ROI diameter of 10 pixels (4.5 mm). The results show a substantial difference between the SNR and CNR values of the phantom images. For all evaluated ROIs at tube voltages of 80, 100, and 120 kV, the SNR values were considerably lower than the corresponding CNR values.

Table 3. SNR and CNR values of the fabricated chest phantom with a simulated lung cancer lesion

Parameters	Voltage (kV)	ROI					Average
		1	2	3	4	5	
SNR	80	0.96	0.64	0.39	1.90	1.96	1.17
	100	2.51	2.55	2.74	3.83	6.02	3.53
	120	3.07	2.71	2.77	1.76	6.75	3.41
CNR	80	32.62	28.59	24.91	36.88	40.97	32.79
	100	40.82	34.91	34.93	34.14	33.38	35.64
	120	43.07	42.88	40.36	31.43	60.50	43.65

Table 3 shows that the SNR values at all tube voltages (80, 100, and 120 kV) ranged from 0.39 to 6.75, whereas the CNR values ranged from 24.91 to 60.50. At 80 kV, the SNR values ranged from 0.96 to 1.96, with CNR values ranging from 24.91 to 40.97. At 100 kV, the SNR values increased to 2.51 to 6.02, with CNR values ranging from 33.38 to 40.82. At 120 kV, the SNR values ranged from 1.76 to 6.75, while the CNR values ranged from 31.43 to 60.50. The highest SNR and CNR values were obtained at ROI 5 at 120 kV, with values of 6.75 and 60.50, respectively.

Figure 6 shows the variation in SNR and CNR values across five slices for the three tube voltages (80, 100, and 120 kV). Increasing the tube voltage to 120 kV increased the CNR values for

ROI 1, ROI 2, ROI 3, and ROI 5. However, the CNR value for ROI 4 decreased from 36.88 at 80 kV to 31.43 at 120 kV. These differences in values are related to the parameters used. SNR evaluates the ratio of the signal to noise within a single ROI, whereas CNR evaluates the difference in signal between the object and reference ROIs relative to noise, resulting in higher CNR values than SNR values.

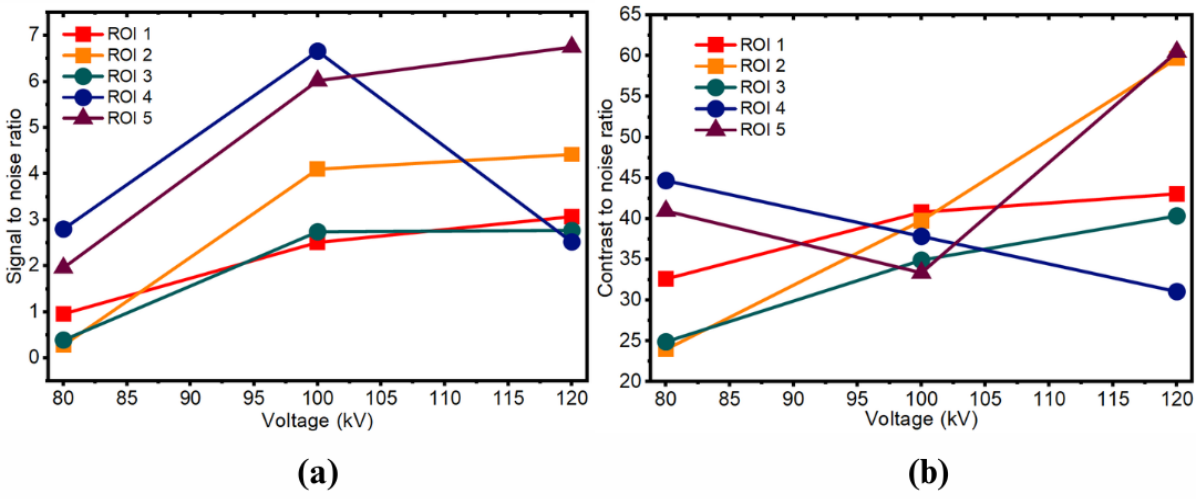


Figure 6. The graphs of SNR and CNR from the chest phantom: (a) SNR and (b) CNR

3.2 Discussions

The high prevalence of lung cancer among adults highlights the importance of radiation dose optimization. Chest phantoms can serve as substitute objects for patients during radiation dose optimization studies. This study aimed to develop a chest phantom that is more affordable and accessible by using materials that are readily available on the market. The results showed that the CT numbers of PMMA, $CaCO_3$ derived from *Anadara antiquata* shell waste, and PU foam in the fabricated phantom were within the CT number ranges of soft tissue, bone, and normal lung tissue based on both reference values and patient reference images. In contrast, the PU foam cavity created to accommodate the beeswax insert exhibited a CT number that differed substantially from that of the lung cancer lesion.

The CT number measured in the lung region can be used to evaluate the attenuation characteristics of the simulated lung lesion within the phantom (Nisa et al., 2025). On CT images, lung cancer is generally evaluated based on its attenuation characteristics and morphology. As shown in Table 2, beeswax was used as a lesion-substitute material to simulate the radiological attenuation characteristics of pathological tissue within the lungs. Based on CT number measurements using an ROI positioned within the beeswax region, excluding the surrounding PU foam, a CT number of -62.59 ± 17.59 HU was obtained. This CT number falls within the literature-reported range for lung lesion attenuation (−100 to 200 HU) (Swensen et al., 2000; Choi et al., 2019). As shown in Figure 5, the axial phantom images reveal a clearly distinguishable lesion region. It should be noted that the assessment of morphological characteristics, such as part-solid nodules, requires visual evaluation of CT images. Therefore, attenuation values were used to objectively characterize the physical attenuation properties of the material without generalizing the findings to a clinical diagnosis.

Table 3 and Figure 6 show changes in the SNR and CNR values across five chest phantom image slices at different tube voltages (80, 100, and 120 kV). The SNR values ranged from 0.39 to 6.75, whereas the CNR values ranged from 24.91 to 60.50. The mean SNR values at 80, 100, and 120 kV were 1.17, 3.53, and 3.41, respectively. Meanwhile, the corresponding mean CNR values were 32.79, 35.64, and 43.65, respectively. Based on the measurements, a tube voltage of 100 kV yielded the highest mean SNR, whereas 120 kV produced the highest mean CNR. The maximum SNR and CNR values were obtained at ROI 5 at 120 kV, with SNR and CNR values of 6.75 and 60.50, respectively. These results indicate that image quality based on SNR and the ability to distinguish the nodule from the background based on CNR do not necessarily correspond to the same tube voltage condition. The trend

of increasing CNR with increasing tube voltage observed in this study is consistent with the findings reported by Dewi et al. (2022). Meanwhile, the SNR variation observed at 100 kV is consistent with the findings of Tang et al. (2012) regarding SNR characteristics at intermediate tube voltages.

The differences in SNR and CNR values presented in Table 3 represent different aspects of image quality. SNR describes the ratio of signal to noise, whereas CNR describes the difference in signal between the object and the background relative to noise. In this study, each value was calculated using a pair of ROIs placed on the nodule and the background region outside the nodule. Therefore, the CNR can be substantially higher than the SNR when the difference in CT number between the nodule and background is greater than the variation in background noise.

Figure 6 shows that the responses of SNR and CNR to increasing tube voltage were not uniform across all slices. The CNR values from 80 kV to 120 kV increased in slices 1, 2, 3, and 5, from 32.62 to 43.07, from 28.59 to 42.88, from 24.91 to 40.36, and from 40.97 to 60.50, respectively. In contrast, the CNR value in slice 4 decreased from 36.88 at 80 kV to 31.43 at 120 kV. The SNR values also varied among slices; for example, the SNR in slice 5 increased from 1.96 at 80 kV to 6.75 at 120 kV, whereas that in slice 4 decreased from 1.90 at 80 kV to 1.76 at 120 kV. These differences indicate that increasing the tube voltage does not necessarily result in a linear increase in SNR and CNR at every location (Alikhani et al., 2017; Goo, 2012).

Both SNR and CNR are directly proportional to image quality; higher SNR and CNR values indicate better image quality (Dance et al., 2014). As shown in Table 3 and Figure 6, the SNR and CNR variations observed in the chest phantom indicate a stable imaging response to changes in tube voltage. The highest CNR value reached 60.50, indicating that the phantom provided substantial object-to-background contrast relative to the surrounding PU foam, supporting its potential application in CT image quality assessment. Image quality evaluation using SNR and CNR is a standard approach for assessing medical imaging performance across variations in scanning parameters (Greffier et al., 2016; Miftahuddin et al., 2024). As observed in the study results, the highest SNR and CNR values do not necessarily occur at the same tube voltage. This phenomenon can be explained by the physical mechanisms governing the interactions among signal, tissue contrast, and background noise across different X-ray energy spectra. In contrast, CNR depends strongly on the contrast difference between the beeswax lesion and the background lung parenchyma (PU foam). At lower tube voltages, the photoelectric effect becomes more pronounced, resulting in higher object contrast, which can maximize CNR values despite higher image noise levels. At higher tube voltages, a substantial reduction in noise can shift the optimal point for achieving the maximum SNR. Therefore, the complex interactions among photon flux, material attenuation characteristics, and beam-hardening phenomena result in the optimal conditions for peak SNR and CNR performance occurring at different tube voltages (Greffier et al., 2016; Miftahuddin et al., 2024).

The phantom nodule fabricated from beeswax exhibited a measurable signal difference relative to the background across all tested tube voltages. The CNR values ranged from 24.91 to 60.50 at tube voltages of 80, 100, and 120 kV, providing a quantitative profile of object-to-background contrast relative to the surrounding PU foam. The novelty of this study lies in the utilization of $CaCO_3$ derived from *Anadara antiquata* shell waste as a bone component and beeswax as a nodule component in the chest phantom, along with the quantitative evaluation of SNR and CNR responses across three tube voltage variations. Nevertheless, diagnostic detectability cannot be established solely on the basis of CNR magnitude without incorporating observer-based studies or validated clinical threshold criteria. Therefore, this study is positioned as an initial stage of physical evaluation, with further validation of visual and clinical aspects by radiologists required in subsequent stages.

The use of materials such as *Anadara antiquata* shell waste and beeswax in chest phantom fabrication successfully reduced the total fabrication cost to USD 146. This cost is substantially lower than that of commercially available anthropomorphic chest phantoms, which typically cost thousands of US dollars, making the developed phantom a highly affordable alternative for research and calibration purposes. When compared with previous studies on thoracic phantom development (Amini et al., 2018; Jamal et al., 2020; Heryani et al., 2020; Pengpan et al., 2022; Mohammed Ali & Al-Murshedi, 2023; Khallouqi et al., 2024a; and Khallouqi et al., 2024b), those study demonstrates advantages in terms of

cost and the ease of reproducing nodule-shaped lesions using beeswax, while maintaining HU values that closely approximate the literature-reported ranges for human tissues. Nevertheless, the scientific interpretation of this study should be approached with appropriate caution. This study has several important limitations, including the lack of directly acquired clinical images from human patients for analysis, as the evaluation was based exclusively on comparisons with reference attenuation data reported in the literature. Therefore, claims regarding the clinical simulation of lung cancer and the potential for CT dose optimization are strictly limited to the experimental scope of an in-house physical phantom and do not yet reflect the full variability of clinical anatomy. To strengthen future validation, further studies are recommended to include direct comparisons with CT images from adult patients with lung cancer, involve larger patient cohorts and a wider range of tube voltage and current settings, and supplement the analysis of the chemical composition of the bone-equivalent material using Fourier-transform infrared spectroscopy (FTIR). Phantom validation should also incorporate existing standard phantoms to broaden the scope and diversity of the research findings.

4. CONCLUSION

This study successfully fabricated a chest phantom using readily available materials at a total fabrication cost of USD 146. The developed phantom demonstrated the potential to approximate established literature-derived CT characteristics of human thoracic tissue, including cancerous lesions, soft tissue, ribs (bone), and normal lung tissue. The CT numbers of the cancer lesion, normal lung, soft tissue, and bone in the phantom were -62.59 ± 17.59 HU (beeswax), -915.34 ± 15.65 HU, 113.48 ± 14.64 HU, and 1155.35 ± 170.70 HU, respectively. Nevertheless, clinical equivalence has not yet been established, and further refinement of the lesion formulation is required to more accurately replicate the clinical variability of lung cancer in adult patients.

AUTHOR CONTRIBUTIONS

A.A: Visualization, Validation, Methodology, Formal analysis, Data curation; CA: Writing – original draft, Validation, Supervision, Formal analysis; IA: Resources, Methodology, Data curation; NSZ: Writing – validation, Supervision, Formal analysis; HS: Writing – review and editing, Writing – original draft, Supervision, Funding acquisition, Conceptualization.

FUNDING

This research was funded by the Indonesia Endowment Fund for Education (LPDP), Ministry of Finance of the Republic of Indonesia.

CONFLICTS OF INTEREST

The authors declare no conflict of interest.

ARTIFICIAL INTELLIGENCE (AI) USAGE DECLARATION

During the preparation of this manuscript, the authors used ChatGPT (GPT-6) to assist with grammatical corrections. After using this tool, the authors checked, reviewed, and edited the content as necessary to ensure appropriate grammar and language usage.

REFERENCE

Alikhani, B., Jamali, L., Raatschen, H. J., Wacker, F., & Werncke, T. (2017). Impact of CT parameters on the physical quantities related to image quality for two MDCT scanners using the ACR accreditation phantom: A phantom study. *Radiography*, *23*(3), 202–210. https://doi.org/10.1016/j.radi.2017.03.013

Amini, I., Akhlaghi, P., & Sarbakhsh, P. (2018). Construction and verification of a physical chest phantom from suitable tissue equivalent materials for computed tomography examinations. *Radiation Physics and Chemistry*, *150*, 51–57. https://doi.org/10.1016/j.radphyschem.2018.04.020

Anderson, I. J., & Davis, A. M. (2018). Incidental Pulmonary Nodules Detected on CT Images. *JAMA - Journal of the American Medical Association*, *320*(21), 2260–2261. https://doi.org/10.1001/jama.2018.16336

Bushberg, J. T., Seibert, J. A., Leidholdt, E. M., Jr., & Boone, J. M. (2012). *The essential physics of medical imaging* (3rd ed.). Lippincott Williams & Wilkins.

Choi, Y., Gil, B. M., Chung, M. H., Yoo, W. J., Jung, N. Y., Kim, Y. H., Kwon, S. S., & Kim, J. (2019). Comparing attenuations of malignant and benign solitary pulmonary nodule using semi-automated region of interest selection on contrast-enhanced CT. *Journal of Thoracic Disease*, *11*(6), 2392–2401. https://doi.org/10.21037/jtd.2019.05.56

Dance, D. R., Christofides, S., Maidment, A. D. A., McLean, I. D., & Ng, K. H. (2014). Diagnostic Radiology Physics. In *International Atomic Energy Agency (IAEA)*. https://doi.org/10.1201/9781482266641

Dewi, P. S., Ratini, N. N., & Trisnawati, N. L. P. (2022). Effect of x-ray tube voltage variation to value of contrast to noise ratio (CNR) on computed tomography (CT) Scan at RSUD Bali Mandara. *International Journal of Physical Sciences and Engineering*, *6*(2), 82–90. https://doi.org/10.53730/ijpse.v6n2.9656

Frellesen, C., Kaup, M., Wichmann, J. L., Hüsers, K., Scholtz, J. E., Albrecht, M. H., Metzger, S. C., Bauer, R. W., Kerl, J. M., Lehnert, T., Vogl, T. J., & Bodelle, B. (2016). Noise-optimized advanced image-based virtual monoenergetic imaging for improved visualization of lung cancer: Comparison with traditional virtual monoenergetic imaging. *European Journal of Radiology*, *85*(3), 665–672. https://doi.org/10.1016/j.ejrad.2015.12.022

Fu, W., Sharma, S., Solomon, J., Ria, F., Setiawan, H., Ding, A., Segars, W. P., & Samei, E. (2025). Patient-specific organ dose and in-vivo image quality assessment in clinical CT. *Physica Medica*, *136*(June). https://doi.org/10.1016/j.ejmp.2025.105017

Goo, H. W. (2012). CT radiation dose optimization and estimation: An update for radiologists. *Korean Journal of Radiology*, *13*(1), 1–11. https://doi.org/10.3348/kjr.2012.13.1.1

Greffier, J., Pereira, F., Macri, F., Beregi, J. P., & Larbi, A. (2016). CT dose reduction using Automatic Exposure Control and iterative reconstruction: A chest paediatric phantoms study. *Physica Medica*, *32*(4), 582–589. https://doi.org/10.1016/j.ejmp.2016.03.007

Hassan, S. U, Abdulkadir, S. J., Fayyaz, A. M., Al-Selwi, S. M., & Ismail, A. O. A. (2026). Interpretable MedDeepNet: Deep feature learning with atom search optimization for explainable lung cancer detection in CT images. *Machine Learning with Applications*, *25*(August). https://doi.org/10.1016/j.mlwa.2026.100973

Heryani, H., Sutanto, H., Anam, C., & Reskianto, A. D. (2020). Development of Synthetic Bones for ANSI Chest Phantom Dosimetry. *European Journal of Advances in Engineering and Technology*, *2020*(9), 2–7.

Hong, D., Moon, S., Seo, J. B., & Kim, N. (2023). Development of a patient-specific chest computed tomography imaging phantom with realistic lung lesions using silicone casting and three-dimensional printing. *Scientific Reports*, *13*(1), 1–9. https://doi.org/10.1038/s41598-023-31142-5

Jamal, N. H. M., Sayed, I. S., & Syed, W. S. (2020). Estimation of organ absorbed dose in pediatric chest X-ray examination: A phantom study. *Radiation Physics and Chemistry*, *166*(September), 108472. https://doi.org/10.1016/j.radphyschem.2019.108472

Kamal, I., Razak, H. R. A., Karim, M. K. A., Mashohor, S., Liew, J. Y. C., Low, Y. J., Zaaba, N. A., Norkhairunnisa, M., & Rafi, N. A. S. M. (2022). Mechanical and Imaging Properties of a Clinical-Grade Kidney Phantom Based on Polydimethylsiloxane and Elastomer. *Polymers*, *14*(3). https://doi.org/10.3390/polym14030535

Khallouqi, A., Halimi, A., & El rhazouani, O. (2024a). Comparative dosimetry of an epoxy resin pediatric head phantom and PMMA phantom for CT imaging. *Radiation Physics and Chemistry*, *216*(May 2023), 111350. https://doi.org/10.1016/j.radphyschem.2023.111350

Khallouqi, A., Halimi, A., & El rhazouani, O. (2024b). Evaluating polyester resin as a viable substitute for PMMA in computed tomography dosimetry phantoms. *Nuclear Engineering and Technology*, *56*(9), 3758–3763. https://doi.org/10.1016/j.net.2024.04.024

Larke, F. J., Kruger, R. L., Cagnon, C. H., Flynn, M. J., McNitt-Gray, M. M., Wu, X., Judy, P. F., & Cody, D. D. (2011). Estimated radiation dose associated with low-dose chest CT of average-size participants in the national lung screening trial. *American Journal of Roentgenology*, *197*(5), 1165–1169. https://doi.org/10.2214/AJR.11.6533

McCollough, C. H., Primak, A. N., Braun, N., Kofler, J., Yu, L., & Christner, J. (2009). Strategies for Reducing Radiation Dose in CT. *Radiologic Clinics of North America*, *47*(1), 27–40. https://doi.org/10.1016/j.rcl.2008.10.006

Miftahuddin, D., Prayitno, A. G., Hariyanto, A. P., Gani, M. R. A., & Endarko, E. (2024). Evaluation of low-dose pediatric chest CT examination using in-house developed various age-size pediatric chest phantoms. *European Journal of Radiology*, *177*(February), 1–9. https://doi.org/10.1016/j.ejrad.2024.111599

Mohammed Ali, A., & Al-Murshedi, S. (2023). Low-cost chest paediatric phantom for dose optimisation: construction and validation. *Radiologia*, *65*(4), 327–337. https://doi.org/10.1016/j.rx.2022.11.011

Nathan, V., Prithishkumar, I., & Livingstone, R. (2021). Estimation of anatomical dimensions of the thorax from computed tomography images of the adult and pediatric Indian population for developing optimal radiological protocols. *Journal of Medical Physics*, *46*(4), 295–299. https://doi.org/10.4103/jmp.JMP_19_21

Nisa, K. A., Anam, C., Alkian, I., Naufal, A., & Sutanto, H. (2025). Design and fabrication of paediatric chest phantom using polymethyl methacrylate-polyurethane foam for pneumonia imaging evaluation. *Radiation Physics and Chemistry*, *232*(November 2024). https://doi.org/10.1016/j.radphyschem.2025.112610

Novitasari, D., Anam, C., Setiawati, E., Amilia, R., Naufal, A., & Reskianto, A. D. (2024). Evaluation of IndoQCT for automatic measurement of contrast-to-noise ratio (CNR) on American college of radiology (ACR) CT phantom images. *AIP Conference Proceedings*, *3210*(1). https://doi.org/10.1063/5.0228091

Pengpan, T., Rattanarungruangchai, N., Dechjaithat, J., Panthim, P., Siricharuwong, P., & Prapan, A. (2022). Optimization of Image Quality and Organ Absorbed Dose for Pediatric Chest X-Ray Examination: In-House Developed Chest Phantom Study. *Radiology Research and Practice*, *2022*, 1–10. https://doi.org/10.1155/2022/3482458

Pratama, N. G., & Widayanti, A. (2025). Karakteristik Limbah Cangkang Kerang Bulu dan Material Alam sebagai Campuran Perkerasan pada Lapis Asphalt Concrete-Wearing Course (AC-WC). *Jurnal Media Publikasi Terapan Transportasi*, *3*(3), 240–246. https://doi.org/10.26740/mitrans.v3n3.p240-246

QRM GmbH. (2020). *Thorax/abdomen phantom specifications* [Product specification sheet]. QRM GmbH - A PTW Company.

Rahmawati, T. N., Anam, C., Setiawati, E., Amilia, R., Naufal, A., & Widhianto, R. W. (2024, August). Evaluation of contrast-to-noise ratio measurements using IndoQCT on images of the American association of physicists in medicine (AAPM) CT performance phantom. In *AIP Conference Proceedings* (Vol. 3210, No. 1, p. 030007). AIP Publishing LLC. doi: https://doi.org/10.1063/5.0228089

Rodgers, S., Atkinson, J., Cryer, D., Storm, C., Nezich, R., Ebert, M. A., & Rowshanfarzad, P. (2024). Construction and validation of an infant chest phantom for paediatric computed tomography. *Physical and Engineering Sciences in Medicine*, *47*(2), 491–501. https://doi.org/10.1007/s13246-023-01379-5

Sawall, S., Maier, J., Ziener, C. H., Schlemmer, H. P., Do, T. D., Kauczor, H. U., Schoenberg, S. O., Froelich, M. F., & Kachelrieß, M. (2025). Lung cancer screening CT acquisition protocols for three generations of CT systems conforming to German legislation. *Physica Medica*, *139*(September). https://doi.org/10.1016/j.ejmp.2025.105208

Sergi, C., Sarasini, F., & Tirillò, J. (2022). The compressive behavior and crashworthiness of cork: A review. *Polymers*, *14*(1). https://doi.org/10.3390/polym14010134

Sookpeng, S., Cheebsumon, P., Pengpan, T., & Martin, C. (2016). Comparison of computed tomography dose index in polymethyl methacrylate and nylon dosimetry phantoms. *Journal of Medical Physics*, *41*(1), 45–51. https://doi.org/10.4103/0971-6203.177287

Sung, H., Ferlay, J., Siegel, R. L., Laversanne, M., Soerjomataram, I., Jemal, A., & Bray, F. (2021). Global Cancer Statistics 2020: GLOBOCAN Estimates of Incidence and Mortality Worldwide for 36 Cancers in 185 Countries. *CA: A Cancer Journal for Clinicians*, *71*(3), 209–249. https://doi.org/10.3322/caac.21660

Swensen, S. J., Viggiano, R. W., Midthun, D. E., Müller, N. L., Sherrick, A., Yamashita, K., Naidich, D. P., Patz, E. F., Hartman, T. E., Muhm, J. R., & Weaver, A. L. (2000). Lung nodule enhancement at CT: Multicenter study. *Radiology*, *214*(1), 73–80. https://doi.org/10.1148/radiology.214.1.r00ja1473

Tang, K., Wang, L., Li, R., Lin, J., Zheng, X., & Cao, G. (2012). Effect of low tube voltage on image quality, radiation dose, and low-contrast detectability at abdominal multidetector CT: Phantom study. *Journal of Biomedicine and Biotechnology*, *2012*(Lcd). https://doi.org/10.1155/2012/130169

World Health Organization (2023). WHO - Lung cancer. https://www.who.int/newsroom/fact-sheets/detail/lung-cancer. (Accessed 06 October 2026).